On the seasonality of waters below the seasonal thermocline in the Gulf of Cádiz

R.F. Sánchez-Leal [a,*], M.J. Bellanco [a], C. Naranjo [b], J. García-Lafuente [b], C. González-Pola [c]

[a] Spanish Institute of Oceanography. Cádiz Center. Puerto Pesquero, Muelle de Levante, s/n, E11006. Cádiz, Spain
[b] Physical Oceanography Group. Instituto de Biotecnología y Desarrollo Azul, IBYDA, University of Málaga, Campus de Teatinos, E29071, Málaga, Spain
[c] Spanish Institute of Oceanography. Gijón Center. Avenida Príncipe de Asturias, 70 bis, E33212, Gijón, Asturias, Spain

A B S T R A C T

This work examines the seasonal thermohaline variability in the Gulf of Cádiz (SW Iberian Peninsula) based on 2009–2020 repeated hydrographic observations. Subsurface water types are assorted within the mixing triangle formed by Mediterranean and Eastern North Atlantic Central Waters (ENACW). A sharp interface between 400-500 m depth separates the saline Mediterranean Overflow Waters (MOW) from the ENACW salinity minimum siting atop. The water column is warmer and more saline in winter (cooler, fresher in summer). Maximum differences of up to 0.6 °C and 0.15 emanate from the ENACW/MOW interface. Changes appear related to the wind-driven seasonal alternation of vertical displacement of isopycnals and poleward-equatorward transports. Upwelling-favorable winds in summer steer positive Ekman pumping velocities, which seem responsible for cooling over the ENACW salinity minimum. Below, the warm, saline signal of subtropical waters from the Azores current is attenuated by the summer approach of cooler, fresher waters from the Portugal Current system. The change of sign of Ekman pumping in winter suggests subsidence of isopycnals and warming/salinification under the seasonal thermocline. Seasonal thermohaline changes of waters leaving the Medi-terranean Sea are insufficient to explain the variations under the ENACW/MOW interface. Rather, variability of Atlantic waters entrained by the overflow seem to dictate these differences.

1. Introduction

The Gulf of Cádiz (GoC) opens to the Atlantic Ocean at 9°W, between capes St. Vincent (SW Iberian Peninsula) and Beddouza (NW Africa) (Fig. 1). Unlike most bays, the enclosed margin is dissected by an oceanic gateway, the Strait of Gibraltar (SoG). The SoG conducts the two-layer water exchange between the Mediterranean and the Atlantic. Eastern North Atlantic Waters (ENACW) from both the Azores and the Portugal Current System (Carracedo et al., 2014, Fig. 1), seasonally modified by local air-sea interactions, feed the surface Atlantic Jet into the Alborán Sea (Peliz et al., 2013). Underneath, a blend of up to four saline Mediterranean waters (MedW: these are distinct water masses brewed across the Mediterranean basin; mostly composed by Levantine Intermediate Water, LIW) are mixed with the overlying Atlantic waters throughout the SoG to produce about 1 Sv ð1*Sv* ¼ 10^6 m^3s^{-1}Þ of dense Mediterranean Overflow Water (MOW; see Naranjo et al., 2015, for a recent review). Past the Spartel Sill (westernmost fringe of the SoG), the MOW cascades into the GoC as a gravity current (Sánchez-Leal et al., 2017) under the lighter ENACW. (In this paper we use the term *MOW* to refer to the water mass produced across the GoC by entrainment of Atlantic waters into the *pure* MedW that cross the SoG.)

The MOW current initially flows westward attached to the continental slope. On its rugged journey (Sánchez-Leal et al., 2017), it descends (from 200 at the SoG to 1000 m off the Cape St. Vincent), splits horizontally in several branches and detaches from the ground as it spreads in the vertical as a turbulent plume (thickness goes from 150 to 800 m). By 9°W it has tripled its volume transport due to turbulent mixing and entrainment with ambient waters (Baringer and Price, 1997). The final MOW mix is composed by 34% MedW, 57% ENACW and 8% of a very diluted (modified) form of Antarctic Intermediate water (mAAIW; *e.g* Louarn and Morin, 2011), whose presence in the GoC varies seasonally (Roque et al., 2019). This is a two-way process that also steers an upward salt flux (Mauritzen et al., 2001) that is responsible for the horizontal salinity gradients within the ENACW layer (more saline near the SoG; *e.g.*, Sánchez-Leal et al., 2017).

After reaching 9°W, part of the MOW follows the topography around Cape St. Vincent. The remainder enters the Atlantic interior at mid-depths (Iorga and Lozier, 1999). Since hydrological variability in the GoC influences the 3D location, properties and strength of the MOW, it arguably modulates the state of the Atlantic circulation: a warmer, dryer MOW may enhance the Azores current, weaken the Subpolar Gyre and cool the Nordic Seas (and *vice-versa*; Swingedouw et al., 2019). Through

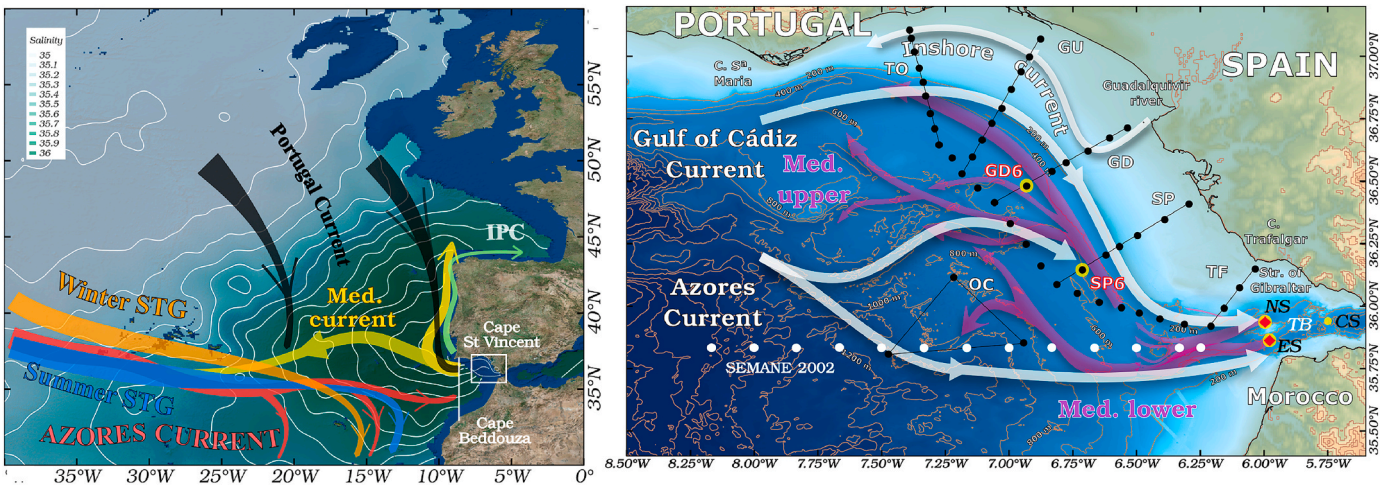

Fig. 1. Left: location of the study area in the subtropical eastern North Atlantic. Contours and shades depict mean salinity at 1200 m. High salinities emanate from the GoC and reveal the impact of the Mediterranean Overflow on the intermediate water mass field. Colored arrows depict the approximate location of the Iberian Poleward (IPC), Portugal, Azores and MOW currents (Carracedo et al., 2014), as well as the winter and summer extension of the North Atlantic Subtropical Gyre (STG; Stramma and Siedler, 1988). The white square encloses the northeastern GoC, enlarged in the right panel. The vertical white line at about 9˚W joins capes St. Vincent and Beddouza. Right: sketch of the regional currents in the northeastern GoC. Light arrows outline the mean surface current field, including the inshore counter-current (Relvas and Barton, 2002), the Gulf of Cádiz Current (GCC; Peliz et al., 2009) and the northern branch of the Azores Current (Peliz et al., 2007). Dark arrows depict the deep Mediterranean currents (Sánchez-Leal et al., 2017). Black dots and black lines indicate the STOCA sampling scheme. Observations began in July 2009 with three hydrographic lines: TF (4 stations off Cape Trafalgar), SP (6 stations off the Sancti-Petri Islet) and GD (6 stations off the Guadalquivir river mouth). The number of stations was enlarged in March 2016 with the addition of TO and GU lines, an offshore station for each of the initial lines and closure stations. The OC group was initiated in December 2018. In this work we use data from SP and GD lines, in particular SP6 and GD6 (highlighted yellow dots). We also use CTD profiles at both the northern (NS) and southern Spartel (ES) channels (western sill of the Strait of Gibraltar). Additional CTD profiles from 35.8˚N line of the SEMANE-2002 cruise (Carton et al., 2010) were used to discuss the choice of suitable source water types. Location of the Tangier Basin (TB) and Camarinal Sill (CS) are also labeled. (For interpretation of the references to color in this figure legend, the reader is referred to the Web version of this article.)

complex mechanisms, such changes may have implications on the Atlantic meridional overturning circulation (van Dijk et al., 2018) and North Atlantic climate (Potter and Lozier, 2004).

There is enough evidence that both Atlantic-Mediterranean exchange and hydrological properties around the GoC have changed over time (*e.g.*, Hernández-Molina et al., 2014). Salinity and temperature reconstructions suggest intense shifts of the MOW following the impact of glacial changes in the Mediterranean Sea (van Dijk et al., 2018). The instrumental record reveals hydrological variability in the subtropical North Atlantic at shorter timescales, with warming and salinification from 1959 to 1981 and cooling and freshening afterwards (Leadbetter et al., 2007). These changes appear controlled by alterations in the source water masses (the MOW among others; Potter and Lozier, 2004) as well as wind-induced circulation turnarounds which may modify the MOW mass distribution and alter the regional hydrology (Bozec et al., 2011). Analogous changes occur at seasonal timescales. Prieto et al. (2013) reported cooler and less saline (warmer and more saline) ENACW around the western Iberian Peninsula in summer (winter), a pattern that is mirrored by the MOW (Millot, 2007; García-Lafuente et al., 2015).

Monitoring and understanding the variability of GoC waters is necessary to estimate and predict potential impacts of timescale MOW variations in the North Atlantic (Swingedouw et al., 2019). This monitoring should include the observation of Atlantic waters, given that they compose up to 2/3 of the final MOW (Sánchez-Leal et al., 2017; Naranjo et al., 2017). With this premise in mind, in 2009 we designed the STOCA Ocean Observing Program to acquire high quality, systematic observa-tions in the eastern GoC. The present paper describes and analyzes these observations. The main objective is the elucidation of mechanisms controlling the seasonal hydrological variability of waters below th seasonal thermocline in the GoC. The paper is organized as follows: section 2 presents the STOCA Program and introduces the dataset and methodology, section 3 displays the results, section 4 contains the dis-cussion of results and the explanation of the intercorrelated responses and feedbacks acting across temporal scales. Conclusions are listed in section 5.

2. Data and methods

2.1. STOCA and GoCaTS programs

Since July 2009 the Spanish Institute of Oceanography (IEO) manages the program *Time Series of Oceanographic data in the GoC* (STOCA, in Spanish). STOCA maintains repeated observations at fixed oceano-graphic stations distributed along five across-shelf transects (Fig. 1, right). STOCA cruises were conducted three times a year from 2009 to 2012, and quarterly on hereafter. Additional hydrographic observations are incorporated since 2013 within the frame of the *Gulf of Cádiz Time- series Study* (GoCaTS), to provide at least 6 observations per year. STOCA/GoCaTS are part of the IEO Observing System (IEOOS, Tel et al., 2016). GoCaTS data are annually presented to the ICES Working Group on Oceanic Hydrography (ICES-WGOH) and contribute to the elabora-tion of the ICES Report on Ocean Climate (González-Pola et al., 2019).

2.2. CTD observations

2.2.1. GoCaTS data

In this work we used CTD observations taken along the SP STOCA line (see Fig. 1 for location details) from 59 STOCA/GoCaTS cruises carried out over 2009–2020. These consisted of full-depth profiles acquired with a factory-calibrated Sea-Bird Electronics SBE 9+ probe. CTD data were processed and controlled following the GO-SHIP guidelines (McTaggart et al., 2010). The monthly distribution of observations was uneven. For instance, SP6 (the outermost station of SP line, at 36.15˚N 6.71˚W; bottom depth: 611 m) had 87 occupations, of which 8 had to be discarded due to instrument malfunction. January, April and May had no observations (Fig. 2). In order to render a reference climatology across each line, we constructed pooled seasonal means from monthly averages. These provided *extended* winter (December, February and March -DFM-), early summer (June, July and August -JJA-) and early autumn (September, October and November –SON–) mean fields. Spring was left out due to the lack of data in April and May (Fig. 2). We

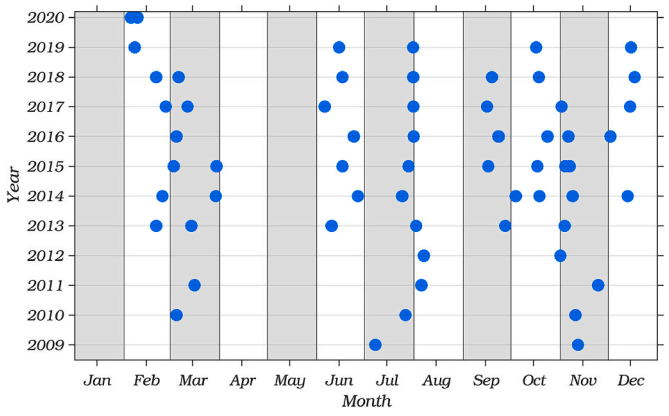

Fig. 2. Temporal distribution of the 79 valid occupations carried out at SP6 over July 2009–February 2020: 12 in February and March, 11 in July, 10 in June, 9 in November, 8 in October, 7 in September, and 6 in August and December. January, April and May had no observations at all.

conducted a similar analysis for GD data (presented in Supplementary Materials). GD is located some 50 km northwest of SP (Fig. 1). The joint study of GD/SP data serves to evaluate the water mass transformation with increasing distance from the SoG, in particular of those transported by the upper MOW.

2.2.2. *Ancillary CTD observations*

In order to define the mean conditions around the study area we also included CTD profiles from other sources than GoCaTS. The bounds of the MedW were delineated with CTD observations acquired at the northern (NS) and southern Spartel (ES) channels (western sill of the Strait of Gibraltar, red squares in Fig. 1, right). These consisted of 27 occupations at NS (2009–2019) and 39 occupations at ES (2011–2020; Fig. 3), the latter conducted during the servicing of the ES mooring line (Sammartino et al., 2015). In addition, CTD profiles across the 35.8°N line of the SEMANE-2002 cruise (Louarn and Morin, 2011) permitted to bound the presence of mAAIW in the GoC.

2.3. *Wind and velocity*

Surface wind and wind stress curl taken from the 0.25-degree Scatterometer Climatology of Ocean Winds (SCOW; Risien and Chelton, 2008) were used to compute the Ekman pumping velocity as $W_{Ek} = \frac{\nabla(\tau)}{\rho f}$, with $\nabla(\tau)$ the wind stress curl, ρ a mean water density (taken as 1028 kg m^{-3}) and f the Coriolis parameter. In addition, state estimates of the seasonal variations of the water column velocity across the SW Iberian Peninsula were provided by the v4 of the ECCO Consortium for Esti-mating the Circulation and Climate of the Ocean (release 2 – clima-tology; Forget et al., 2015).

2.4. *Water masses and water mass fractions*

Main source water types (SWT) present in the eastern GoC are plotted in Fig. 3. These include the upper ENACW (u-ENACW; θ: 18.0, *S*: 36.45) the lower ENACW (l-ENACW; θ: 10.0, *S*: 35.40) (Carracedo et al., 2016) and the MedW at CS (θ: 13.08, *S*: 38.50) (García-Lafuente et al., 2017). All waters below σ_θ~26.40 kg m^{-3} (approximate limit of the surface mixed layer; SML) are distributed within the mixing triangle formed by these SWTs. (Note that the mAAIW definition by Louarn and Morin (2011) situates along the side joining l-ENACW and the MedW.) In a first-order approach, we can quantify the mixing ratio in the ob-servations assuming mass, heat and salt conservation in the mixing tri-angle. Mathematically, we express this as a simple linear system of 3 equations with 3 unknowns (Mamayev, 1975):

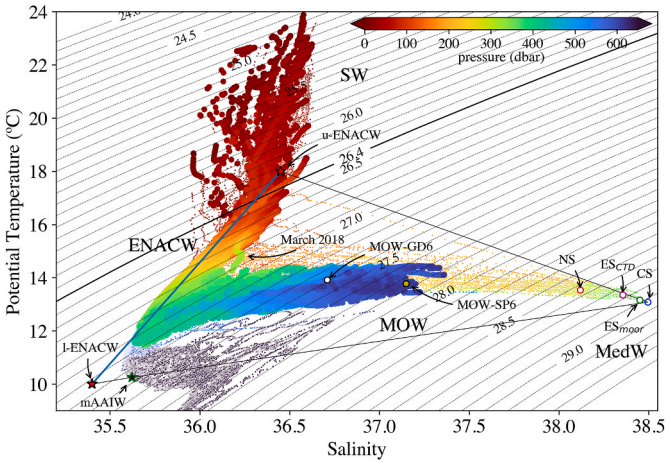

Fig. 3. Scatter plot showing the potential temperature-salinity ($\theta - S$) relationships at SP6, color coded by pressure (heavy dots). Smaller dots represent ancillary observations: very saline types at depths < 350 m are taken at both Spartel channels (NS/ES_{CTD}); SEMANE-2002 observations are visible as cooler, less saline types at depths > 700 m. Observations taken during the development of an anomalously deep SML in March 2018 are labeled. SW indicate the surface water types. The blue straight line marks the typical ENACW relationship, delimited by the $ENACW_{18}$ and $ENACW_{10}$ (Carracedo et al., 2016). The latter (termed u-ENACW and l-ENACW in this paper) are indicated as red stars with black edges. The black star with green edges indicates the mAAIW definition (Louarn and Morin, 2011). Filled circles with colored edges represent several MOW types across the SoC (annotated). From right to left (more to less saline): (blue) Camarinal channel (CS; from García-Lafuente et al., 2017); ES_{moor}(green, from Naranjo et al., 2017); ES_{CTD} (magenta); NS (red); SP6 (green circle with black edge); GD6 (white circle with black edge). ES_{moor} data take the temper-ature minimum in each tidal cycle at the ES mooring as a proxy for the less mixed Mediterranean water flowing out. Values at ES_{CTD}/NS/SP6/GD6 are averages of CTD observations near the bottom (Sánchez-Leal et al., 2017). In this paper we assume that CS hosts the purest MedW. Together with u-ENACW and l-ENACW, it will serve to define the triangle of mixing for the eastern GoC. (For interpretation of the references to color in this figure legend, the reader is referred to the Web version of this article.)

$$\begin{cases} m_1\theta_1 + m_2\theta_2 + m_3\theta_3 = \theta \\ m_1S_1 + m_2S_2 + m_3S_3 = S \\ m_1 + m_2 + m_3 = 1 \end{cases} \quad (1)$$

The water mass contribution of each SWT in the sample (m_i) are the unknowns ($i = (1, 2, 3)$ refer to u-ENACW, l-ENACW and MedW). The exact solution of the linear matrix equation (in the sense that there exists a unique solution to any $\theta - S$ combination within the mixing triangle) can be computed for each observed $\theta - S$ pair. The analysis was done in order to evaluate the seasonal differences in the water mass proportions across SP. More details are provided in the Supplementary Materials.

2.5. *Decomposition of potential temperature and salinity*

CTD observations at SP6 (and GD6, in the Supplementary Materials) were decomposed using the method proposed by Bindoff and McDougall (1994). These stations were chosen because they extended down to the upper MOW (Fig. 1) and are being routinely monitored since the outset of STOCA (Fig. 2). The method assumes that for small displacements, temporal changes of θ on isobars can be separated into two components (Arbic and Owens, 2001):

$$\left.\frac{d\theta}{dt}\right|_p \approx \left.\frac{d\theta}{dt}\right|_n - \left.\frac{dp}{dt}\right|_n \frac{\partial\theta}{\partial p} \quad (2)$$

where p and n indicate changes at isobars and isopycnals, respectively (*e. g.,* Prieto et al., 2013). The left-hand term represents the time variation

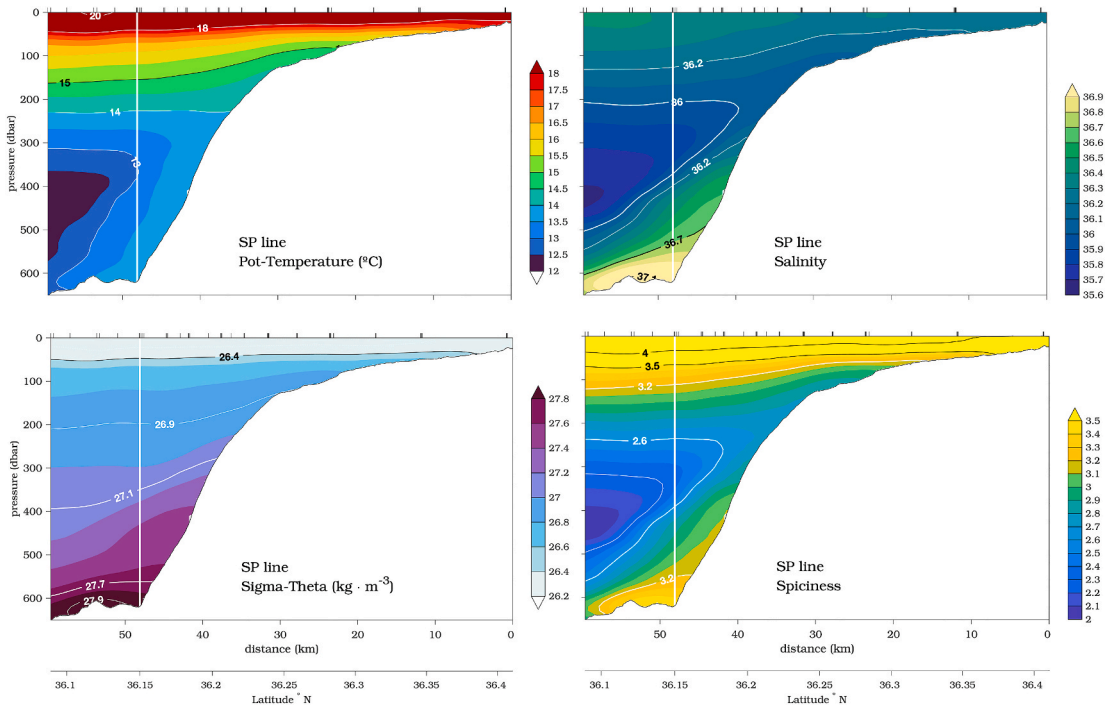

Fig. 4. 2009–2020 mean thermohaline fields across SP. Top panels: potential temperature (left) and salinity (right). Bottom panels: potential density anomaly (left) and spiciness (right). Spiciness is a state variable orthogonal to density in the temperature-salinity space (Flament, 2002). It reflects the passive spatial variations of water-mass properties in density units (McDougall and Krzysik, 2015). It is ideally suited to highlight isopycnal water-mass contrast, which involves a correlation between warm and salty water (versus cool and fresh; Schmitt, 1999). In this sense the MOW is more *spicy* than the cooler, less saline ENACW. Particular contours are depicted for visual aid. Colorbars indicate potential temperature (°C), salinity, potential density anomaly (kg m^{-3}) and spiciness (kg m^{-3}). White vertical lines mark the position of SP6.

of temperature (θ) at isobaric surfaces. If pressure is assimilated to the z-axis, eq. (2) can be simplified as $\theta'_z \approx \theta'_n - N'\theta_z$. The first term on the right-hand of eq. (2) represents (diabatic) changes along isopycnals (or water mass change, interchangeably termed *spice* throughout the text). The second term indicates (adiabatic) changes at pressure levels as a consequence of vertical displacements of isopycnals (termed *heave*). Salinity can be decomposed in a similar manner.

We considered the time-series of differences of each term in eq. (2) with respect to the climatological average constructed from monthly pooled means. Then, time-series of θ and S changes at each pressure level were decomposed to render the corresponding spice and heave contributions. Seasonality was tested by fitting the results to a nonlinear regression model specified by:

$$\psi(t) = asin(2\pi t + b) \tag{3}$$

where a and b are the amplitude and phase of the purely harmonic seasonal cycle, t time in decimal years and 2π the fixed annual frequency. The fit was done using Matlab's *fitnlm* function. The statistical significance of similarities between the detrended time-series and the nonlinear regression model results was checked with *fitnlm* built-in *F-Test*.

3. Results

3.1. Vertical distribution of water masses

The 26.40 kg m^{-3} isopcynal approximately defines the lower limit of the SML at SP6 (Fig. 3). The distinctive presence of upper and lower ENACW emerges as water types following the straight line between u- ENACW and l-ENACW. Comparison of SP6 and SEMANE data reveals the absence of the characteristic bowl-shaped distribution of the cool, low- salinity types associated with the mAAIW. Intense dilution of the MedW in the GoC is the cause that maximum MOW salinities do not exceed 37.4 at SP6.

Fig. 4 discloses the across-shelf distribution of water masses along the SP line. A temperature, salinity and spiciness minimum mark the l-ENACW core. Rising spiciness from that minimum to approximately 100 m depth reveal the increasing presence of the u-ENACW sitting atop. Spiciness also increases down to the seabottom revealing the occupation by the MOW vein. The (arbitrary) choice of the upper and lower 36.0 isohalines (or, alternatively, the 2.6 isospice) helps defining the geom-etry (vertical span between isolines, or thickness) and location (depth) of the l-ENACW core. The upper 36.0 line runs horizontally at about 200 m, but the lower one descends with increasing distance from the shelf- break (Fig. 4), permitting a ticker l-ENACW minimum offshore. The tilt of isohalines below this minimum reveals a l-ENACW/MOW inter-face that also plunges offshore. Observations across the GD line illustrate a similar pattern (Fig. S3, in Supplementary Materials). However, the sharp diminution of salinity gradients across the l-ENACW/MOW interface from SP to GD advocates the existence of active processes promoting coupled transformation of both water masses throughout the MOW pathway (Fig. 1, right panel).

3.2. Seasonal variability of the water column

Temporal variability modulates the static picture shown above. Fig. 5 reveals the impact of extreme events such as the dramatic development of a ≈ 300 m thick SML in March 2018. Focusing on the ENACW layer, the depth of the salinity minimum wiggles on top of a statistically significant soaring trend (56.5 ± 15.1 m in ten years; dashed white line in Fig. 5, top-right panel). In addition, these oscillations are often accompanied by stretching/shrinking of the vertical distance be-tween the 36.0 isohalines (l-ENACW core thickness; black line in Fig. 5, top-right panel). The fit of the l-ENACW core thickness to a seasonal model is not statistically significant. However, the visual inspection permits to observe the recurrent periodicity of a phenomenon that

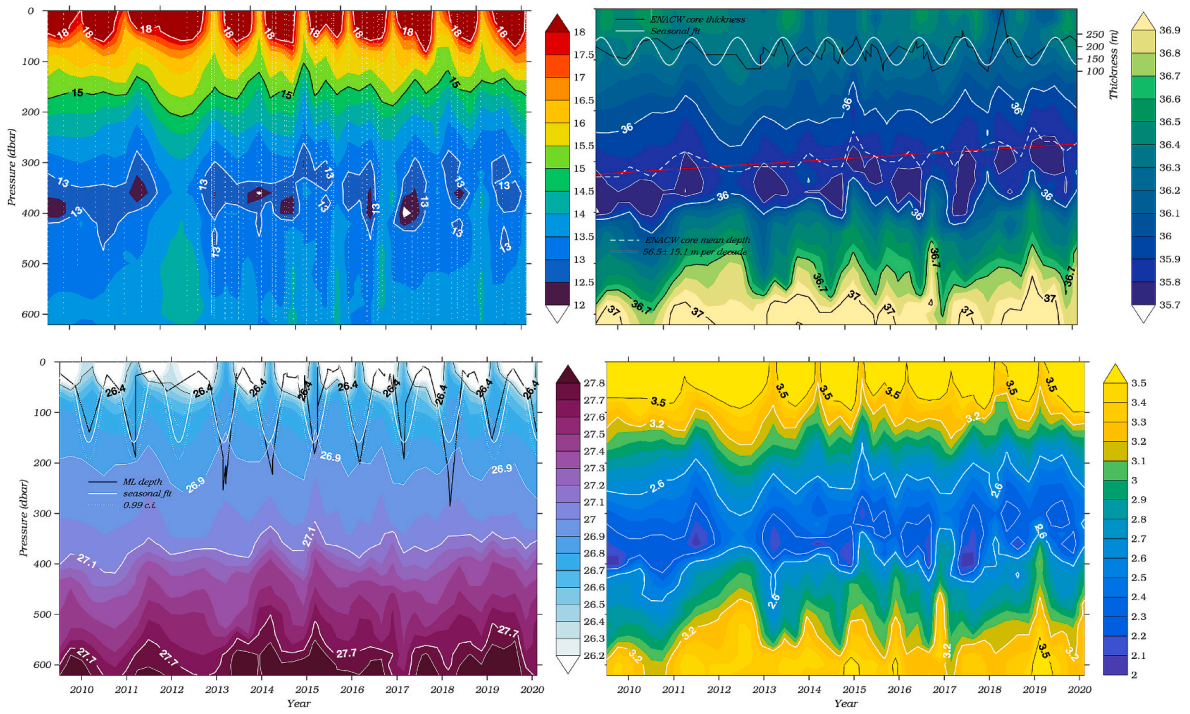

Fig. 5. 2009–2020 evolution of water mass properties at SP6. Top-left panel: Potential temperature (colorbar units are °C). Selected contours are drawn and labeled. Individual vertical profiles are indicated as dotted lines. Top-right panel: Salinity. The 36.0 isohaline outlines the l-ENACW core. Additional contours within the MOW layer have been depicted (in black). The dashed white line represents the l-ENACW core mean depth, computed as the mean depth of the layer with salinity $<$ 36.0. The red line is the linear fit. (The result of the linear fit plus the 0.99 confidence interval was 56.5 $\pm$ 15.1 m per decade.) The evolution of the l-ENACW core thickness in m (taken as the vertical span between the upper and lower 36.0 isohalines) through time (black line) together with a seasonal fit to the observations (white line) is overlaid. Bottom-left panel: Potential density anomaly (colorbar units are kg m^{-3}). Additional isopycnals are outlined in black. Superimposed black line represent the mixed layer depth (MLD), computed as the vertical distance between the surface and the depth at which the density exceeds by 0.125 kg m^{-3} that at the surface. We also included the seasonal fit ($\pm$ the 0.99 confidence intervals, white dashed lines). Bottom-right panel: spiciness (colorbar units are kg m^{-3}). (For interpretation of the references to color in this figure legend, the reader is referred to the Web version of this article.)

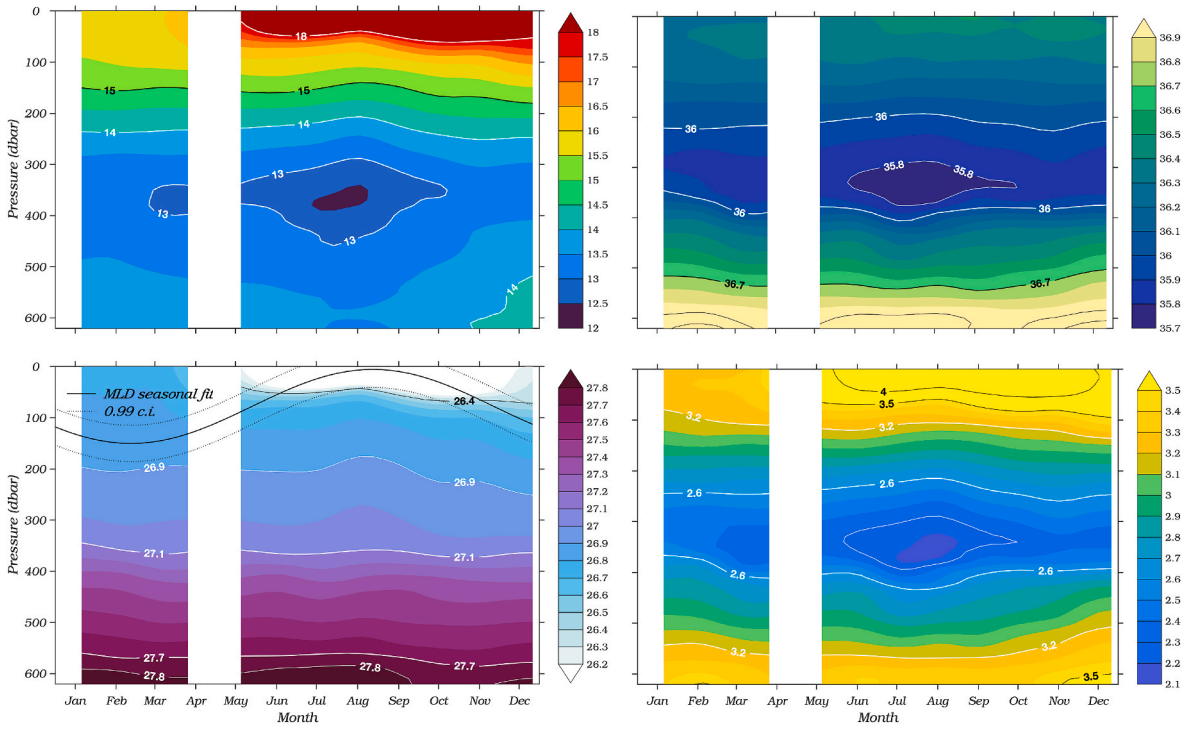

Fig. 6. Seasonal changes at SP6 of water column potential temperature (°C) (top-left panel), salinity (top-right panel), density (kg m^{-3}; bottom-left panel) and spiciness (kg m^{-3}; bottom-right panel) at SP6. The seasonal fit to the MLD is plotted in the bottom-left panel ($\pm$ the 0.99 c.i., black dashed lines).

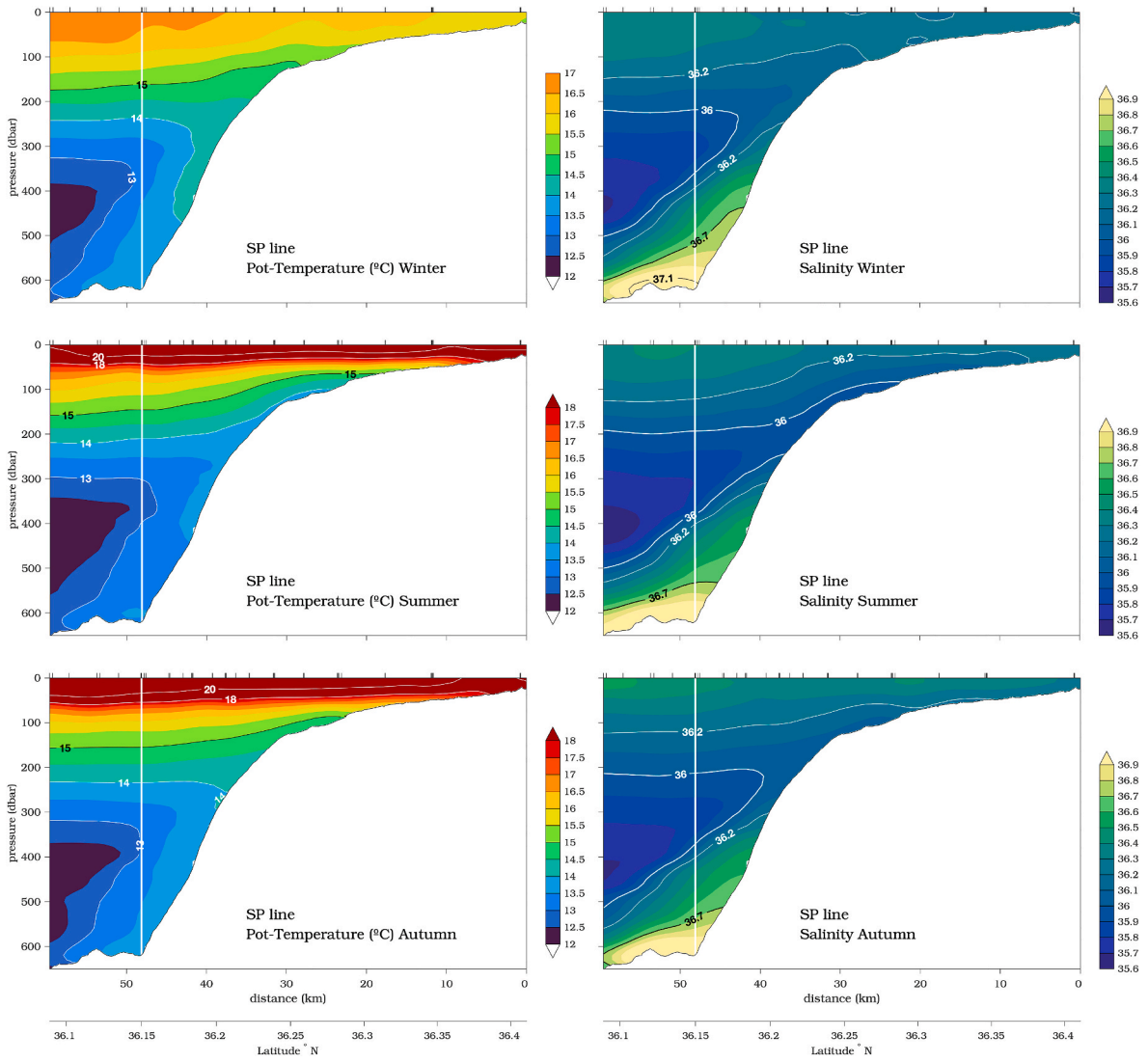

Fig. 7. SP line. 2009–2020 temperature (left panels) and salinity (right panels) means in winter (top), summer (central) and autumn (bottom). Selected contours are depicted for visual aid. Colorbars indicate temperature (˚C) and salinity. White vertical lines mark the location of SP6 in the transect.

features a thicker (by about 120 m) l-ENACW core in summer than in winter (for example between 2016-2018; Fig. 5, top-right panel).

The seasonal seesaw of the ENACW salinity minimum is accompanied by coincident variations of MLD and the l-ENACW/MOW interface depth, suggesting interdependent changes (Fig. 6). Summer restratification and shrinking of the SML, and plunging of the MOW layer below (see the shape of the 36.7 isohaline in the figure) coincides with cooling, freshening and the vertical expansion of the salinity minimum. On the other hand, the formation of a cold SML in winter (about 160 m thick) and soaring of the l-ENACW/MOW interface occurs in phase with warming and salinification of the salinity minimum.

The effect on the cross-sections is illustrated in Fig. 7 (only temperature and salinity are shown). In summer, the salinity minimum spreads in the horizontal and allows relatively fresher and cooler waters on the upper slope. This is evident as waters with salinity below 36.0 smear the upper slope in summer and the 36.7 isohaline sits below 560 m (Fig. 7). In winter the low-salinity wedge retreats offshore as the MOW layer expands laterally. This is noted by the penetration of relatively saline waters onto the upper slope (the 36.0 isohaline does not intersect the bottom and the 36.70 isohaline is about 100 m higher than in summer in Fig. 7). This interplay features coeval seasonal thermohaline changes below the seasonal pycnocline, with cooler, less saline waters in summer (warmer, more saline waters in winter and autumn; Figs. 6 and 7).

3.3. Seasonal variability of the water mass fractions

Seasonal changes illustrated before may stem from changes in the precise depth of the boundaries between different layers or by changes in the water mass properties (including changes in the proportions of the SWTs). One way to detect the latter is by applying a simple mixing model with three SWTs (MedW, l-ENACW and u-ENACW; Fig. 3) and evaluate the winter-summer differences. Results are presented in Fig. 8. The summer thermocline sets a boundary between the surface waters and the u-ENACW. In winter, the MLD extends beyond 150 m depth and permits the transformation of u-ENACW by the mix with surface waters. The MOW layer (salinities > 36.7) features water types with up to 70% of the source MedW. Waters within the salinity minimum layer contain about 50% of the source l-ENACW. Winter-summer differences reveal that, at their respective cores, both the MedW and l-ENACW contribu-tions are very stable year round as no changes greater than 6% occur south of 36.15°N nor below 500 m. While the shape of the MOW layer does not show seasonal changes, the geometry of the l-ENACW core varies considerably. For instance the patch of l-ENACW $> 70\%$ increases its spatial extension in summer. The most striking winter-summer dif-ferences emerge near the seabed from 100 to 500 m. The l-ENACW drop in winter, of more than 12% from 100 to 300 m, contributes to the observed winter warming and salinification on the continental slope

(Bellanco and Sánchez-Leal, 2016).

3.4. Heave and spice components of the seasonal change

The previous section presented the seasonal variability in the eastern GoC from an initial analysis of the observations. Now we focus on SP6 to attempt the identification of steering mechanisms based on the decomposition of changes along isopycnals (spice) and those due to pure heave. Seasonally averaged anomalies (with respect to the annual mean) of the individual decomposition terms, their sum and the isobaric change versus depth are plotted in Fig. 9. Large residuals (discrepancies between sum and the isobaric change) may arise from air–sea in-teractions or in regions where vertical gradients are large (Desbruyères et al., 2014). Time variability within a particular season, such as front shifting, can also result in improbable large vertical velocities or iso-pycnal trends (Arbic and Owens, 2001) that put into question the val-idity of the linear expansion in eq. (2). At SP6, they could be the reason for residuals larger than 30% in the upper 100 m (except for winter salinities) and below 575 m (except for autumn). Otherwise, results support the overall skill of the decomposition method.

Fig. 9 illustrates the winter warming and salinification below 150 m. A relative θ'_z and S'_z maximum occurs between 350-450 m (peak at 380 m, with +0.25 °C and +0.07), which is the approximate location of the l- ENACW core at SP6 (see Fig. 4). Summer features the opposite situation, with cooling and freshening everywhere below 150 m, most intense between 350-450 m (peak at 380 m, with -0.4 °C and -0.11). Autumn accommodates the transition from the cool, relatively fresh summer to the warm, more saline winter. As in winter, the whole water column is warmer than the annual average. However, the water column is more saline only down to approximately 450 m depth, as the isobaric term changes sign and reveals autumn freshening below (including the MOW layer). More interestingly, the autumn warming and salinification fea-tures two separate maxima: from 150 to 350 m (+0.15 °C and +0.03) and between 380-460 m (+0.16 °C and +0.05), the latter particularly conspicuous for salinity.

Fig. 9 shows that changes are steered by a complementary action of heave from 150 to 300 m and spice below. Exception should be made for autumn salinities, where heave overrides spice and pulls the observed changes. Note that in winter (summer), warming/ salinification (cool-ing/freshening) is mainly steered by heave from 150 to 350 m and by spice below. The heave/spice seesaw is nicely illustrated in autumn, when the isobaric changes exhibit a relative minimum at 350 m that separates the heave-dominated part (100–350 m) from the spice- dominated part (350–450 m). The salinity decomposition further sug-gests that heave dominates below 500 m in autumn.

3.5. Annual cycle of isobaric change, spice and heave

Previous sections revealed that spice dominates the variability of the l-ENACW core whereas heave prevails above. These results suggest

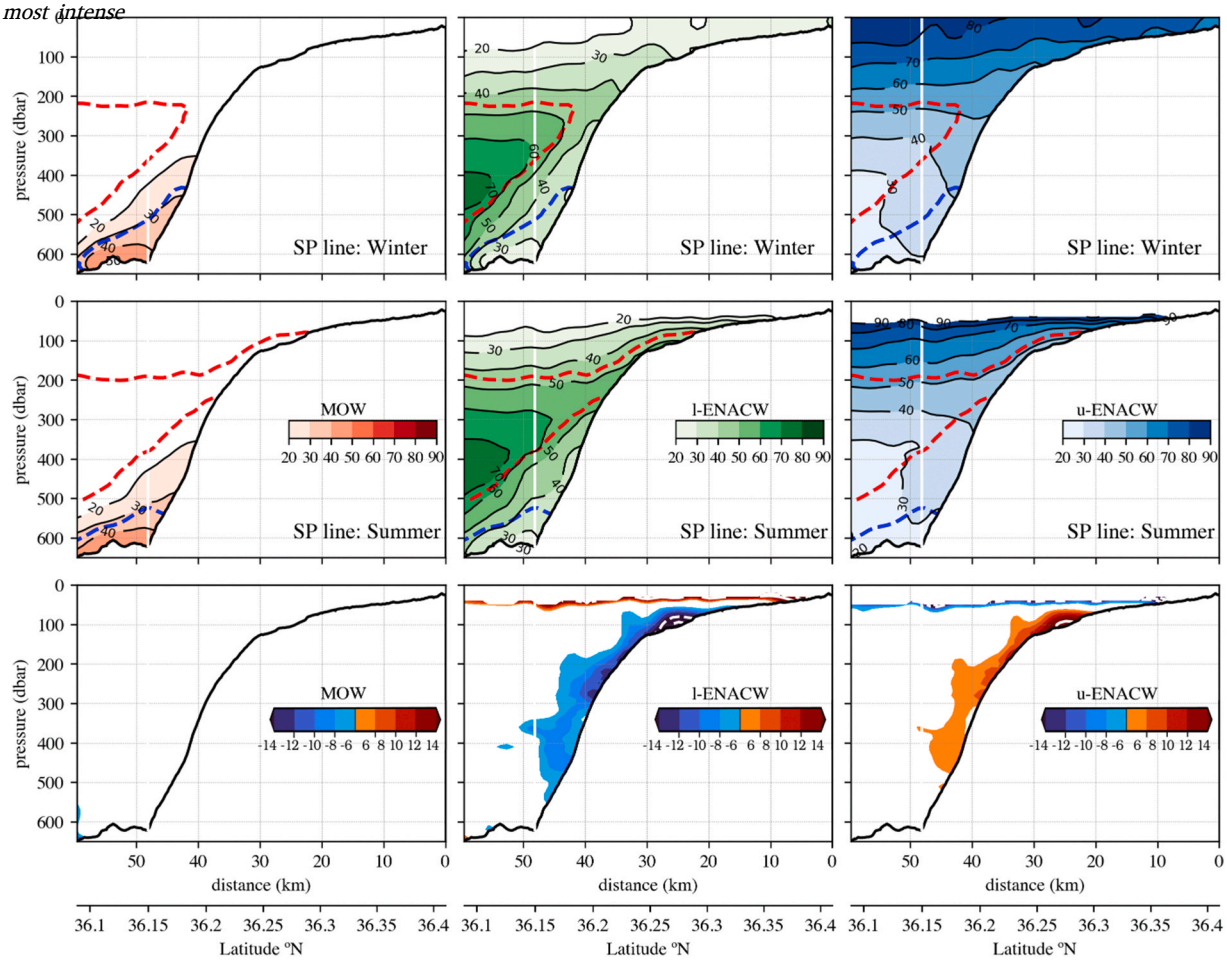

Fig. 8. Contribution (%) of three source water masses (MOW, left panels; l-ENACW, central panels; u-ENACW, right panels) across SP line in winter (top row) and summer (central row). Only shades with contribution greater than 20% are depicted. The bottom row shows winter - summer differences. Only differences greater than 6% are drawn. The vertical white line indicates the location of SP6. The 36.0 (encircling the l-ENACW core; red) and 36.70 (the MOW vein; blue) isohalines are overlaid for reference in the top and central panels. (For interpretation of the references to color in this figure legend, the reader is referred to the Web version of this article.)

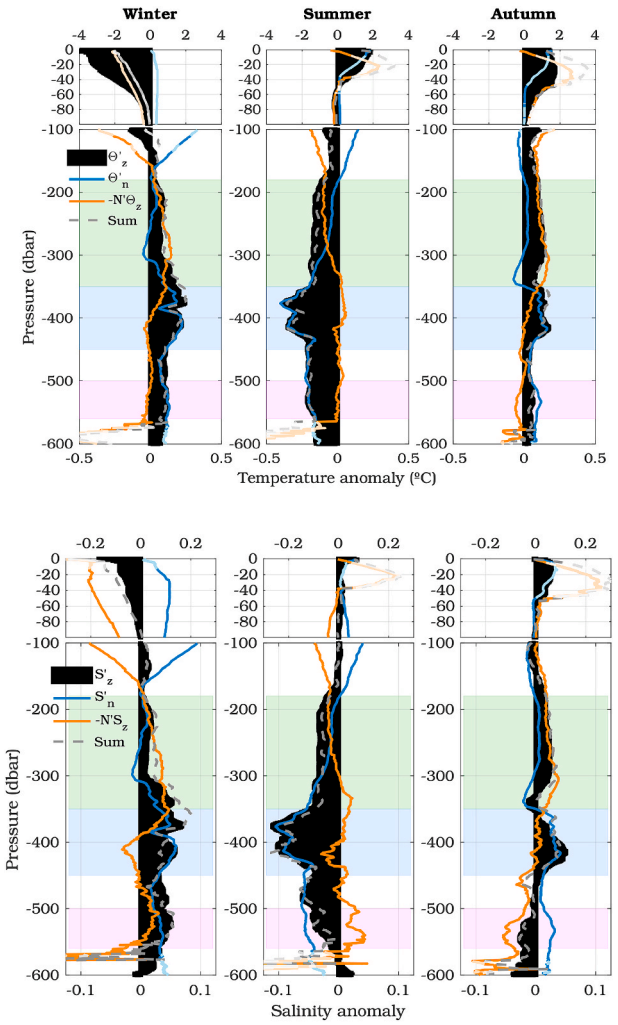

Fig. 9. Seasonal means of terms in eq. (2) versus depth for temperature (top) and salinity (bottom) at SP6. The abscissa uses a different scale for the top 100 m. Black horizontal shades represent the isobaric change (θ'_z and S'_z), the blue line is the isopycnal change (θ'_n and S'_n) and the orange line is heave ($-N'\theta_z$ and $-N'S_z$). The dashed gray line is the sum of isopycnal and heave and should match the isobaric term. Results are dimmed where the difference > 30%. Shaded rectangles mark the l-ENACW core (350–450 m; light blue), the layer immediately above (180–350 m; green) and the top of the MOW vein (500–575 m; magenta). (For interpretation of the references to color in this figure legend, the reader is referred to the Web version of this article.)

dissimilar forcing acting upon each water layer. In order to evaluate the specific contribution to the annual cycle, the detrended isobaric (θ' and S'), spice (θ'_n and S'_n) and heave ($-N'\theta_z$ and $-N'S_z$) were averaged at the depth intervals indicated in Fig. 9. These represented the l-ENACW core (350–450 m), the layer immediately above (180–350 m) and the upper MOW below (500–575 m). The deeper MOW (575–600 m) was left out because the linear decomposition was unsatisfactory. Statisti-cally significant fits to the seasonal model of eq. (3) permitted the reconstruction of the annual cycle (Fig. 10).

The results are summarized in Table 1. Isobaric, isopycnal and heave changes agree for temperature and salinity. Isobaric warming/salinifi-cation occurs in winter (yeardays 7-69) and cooling/freshening in summer. Spice approximately keeps this seasonal cycle (with peaks occurring between yeardays 16-72). Heave acts differently at each depth interval. Above the l-ENACW core, heave resembles the spice cycle and peaks in winter (yeardays 336-348). Below, $-N'\theta_z$ and $-N'S_z$ peak in late spring (yeardays 128-138). The phase shift of heave contributes to the dissimilar characteristics of the annual cycle above and within the l-ENACW core. Heave steers the seasonal temperature changes from 180 to 350 m, with an amplitude of 0.10 ˚C (Fig. 10). Spice dominates the annual l-ENACW thermohaline cycle, featuring an amplitude of 0.22 ˚C (0.06 for salinity). The temperature amplitude across the upper MOW is 0.15 ˚C. Spice is phase-shifted by one-quarter cycle relative to heave. However, the amplitude of the former is larger (0.18 ˚C) and controls the temperature cycle. This phase shift also emerges in the MOW salinity, albeit in this case both terms contribute equally to the annual isobaric cycle (0.05). This is the cause that isobaric salinity lags temperature by one month.

4. Discussion

Of the natural variability, seasonal cycles including annual and semiannual harmonics set the ocean fundamental rhythm (Chen and Wang, 2016). Observations at SP confirm that the GoC is no exception. Surface and subsurface waters exhibit seasonal oscillations that are approximately out of phase with each other. In winter, upper waters are cooler, fresher than the annual average (spicier in summer; Figs. 5–6) while subsurface waters are warmer and more saline (cooler, fresher in summer; Figs. 5 and 10). Whereas the surface variability is a result of local and remote seasonal air-sea fluxes (Bellanco and Sánchez-Leal, 2016), the complementary spice and heave contributions reveal a more complex pattern below.

4.1. ENACW layer

Winter deepening of the MLD (> 150 m; Fig. 5) permits mixing of cool waters from the SML with the u-ENACW. Surface and l-ENACW waters are seldom locally in contact. Only exceptionally the MLD extends across the l-ENACW and down to the MOW layer (such as in March 2018; Fig. 3). Therefore, $\theta - S$ changes of surface and subsurface waters are uncoupled. Our observations reveal warmer and more saline l- ENACW in winter (thicker, cooler and less saline in summer; Fig. 5). Summer cooling is thoroughly observed west of the Iberian Peninsula (García-Lafuente et al., 2015), from the Bay of Biscay (Prieto et al., 2013) to the Strait of Gibraltar (Millot, 2007). Results suggest that changes stem from the overlaid combination of isopycnal and heave controlled fluctuations, and are independent from the dynamics across surface layers. Heave dominates from the base of the SML down to approximately 350 m depth. It is the main contributor to the winter/-autumn warming and salinification and adds to the isopycnal cool-ing/freshening in summer (Fig. 9). Isopycnal changes prevail below, showing a very strong signal centered at 380 m (l-ENACW core), which feature a cold, fresh phase in August (warm, saline in February; Fig. 10).

Vertical velocities in the upper ocean are driven by wind stress curl and the associated Ekman pumping (Liang et al., 2017). In the GoC, wind stress curl is positive year-round and intensifies in summer, the upwelling-favorable season (Fig. 11). ECCO simulations suggest that vertical velocities across the upper 350 m are of the same sign and magnitude as those predicted by Ekman pumping (Fig. 11, bottom-right panel). Heave response in the GoC is synchronous with these wind-driven variations. Enhanced positive wind stress curl in summer boosts the elevation of the l-ENACW core (Sánchez and Relvas, 2003, see their Figs. 3 and 4) and cooling and freshening across the upper 350 m. Upwelling relaxation starting in autumn reduces vertical velocities in this layer, which explains the observed warming and salinification.

Wind-driven seasonal variations of the current system around the eastern subtropical Atlantic ocean provide a mechanism of seasonal isopycnal thermohaline variability below 350 m. Horizontal advection and mixing with waters whose properties changed elsewhere contribute to the renewal of the regional ENACW pool (*e.g.,* Machín et al., 2006; Mason et al., 2011; Carracedo et al., 2014). The seesaw between relaxation-intensification of poleward-equatorward transports may also modulate dynamics of the Azores Current waters into the GoC (Sánchez and Relvas, 2003; Carracedo et al., 2014). The larger east–west and

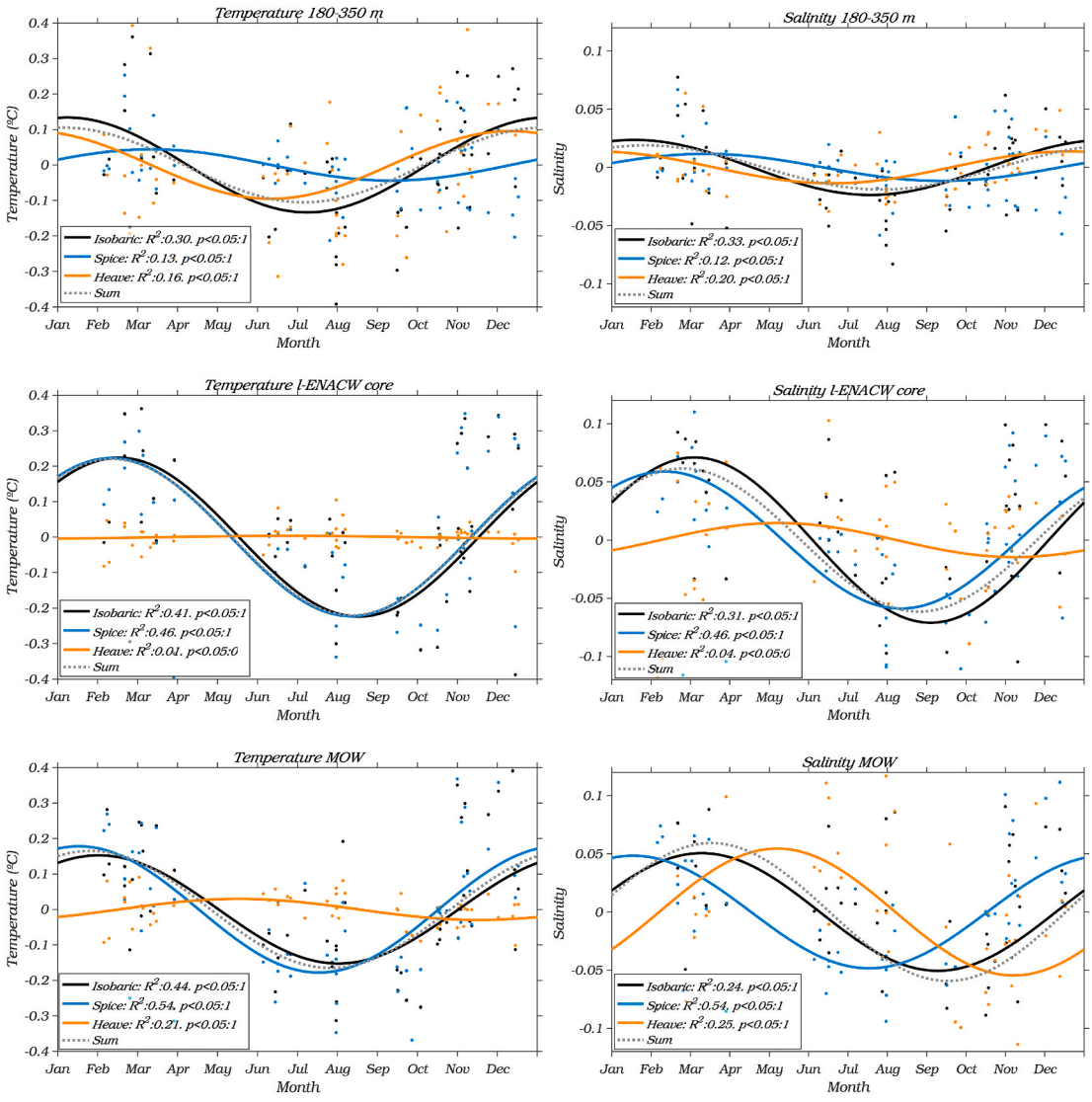

Fig. 10. Annual cycle at SP6 of detrended anomalies of isobaric change (θ'_z and S'_z), spice (θ'_n and S'_n) and heave ($-N'\theta_z$ and $-N'S_z$) averaged over the l-ENACW core (350–450 m; middle row), the layer immediately above (180–350 m; top row) and the upper MOW vein (500–575 m; bottom row). Dots represent the observations and bold lines the responses on the predictors in time using the nonlinear regression model of eq. (3) (the result of a *F-Test* and R^2 is included in top panels). The dashed gray lines depict the sum of spice and heave.

smaller north–south extension of the North Atlantic Subtropical Gyre in summer (Stramma and Siedler, 1988; García-Lafuente et al., 2015) fa-vors the approach of fresher, cooler ENACW towards the western Iberian Peninsula. In addition, upwelling-favorable winds strengthen the coastal branch of the Portugal Current System (Fig. 12) which, in turn, stimulate horizontal advection of cooler, less saline waters into the GoC by coastal upwelling jets (Fig. 1). This process contributes to the occupation of the upper slope by a larger amount of l-ENACW in summer (6–12%; Fig. 8). The situation is probably understated at SP6, which is situated away from the influence of coastal upwelling jets. The alongshore equatorward transport near the Iberian margin shuts down in autumn (Fig. 12, left panel). Poleward flows take over around Cape St. Vincent (Sánchez and Relvas, 2003; Teles-Machado et al., 2015). The end of the upwelling season in autumn is coeval with strengthening of the Azores Current (Fig. 12, left panel) and the transport of a larger amount of spicier subtropical waters into the GoC (Peliz et al., 2009; Carracedo et al., 2014). This alone may explain the observed isopycnal winter warming/salinification at the ENACW level (Fig. 9) and over the shelf break (Fig. 8).

Table 1
Amplitude, phase in yeardays (and calendar month) and R^2 of the nonlinear regression model of eq. (3) applied to the isobaric change, spice and heave. The asterisk indicates where the fit was not statistically significant. The phase indicates the timing of the annual maximum.

	θ' (°C)			θ'_n (°C)			$-N'\theta_z$ (°C)			S'			S'_n			$-N'S_z$		
	a (°C)	b	R^2	a (°C)	b	R^2	a (°C)	b	R^2	a	b	R^2	a	b	R^2	a	b	R^2
180–350 m	0.13	7 (Jan)	0.30	0.04	71 (Mar)	0.13	0.10	336 (Dec)	0.16	0.02	17 (Jan)	0.33	0.01	72 (Mar)	0.12	0.01	348 (Dec)	0.20
l-ENACW core	0.22	47 (Feb)	0.41	0.22	41 (Feb)	0.46	0.00*	129 (May)	0.01	0.07	64 (Mar)	0.31	0.06	41 (Feb)	0.46	0.01*	129 (May)	0.04
Upper MOW	0.15	31 (Jan)	0.44	0.18	16 (Jan)	0.54	0.03	138 (May)	0.21	0.05	69 (Mar)	0.24	0.05	16 (Jan)	0.54	0.05	128 (May)	0.25

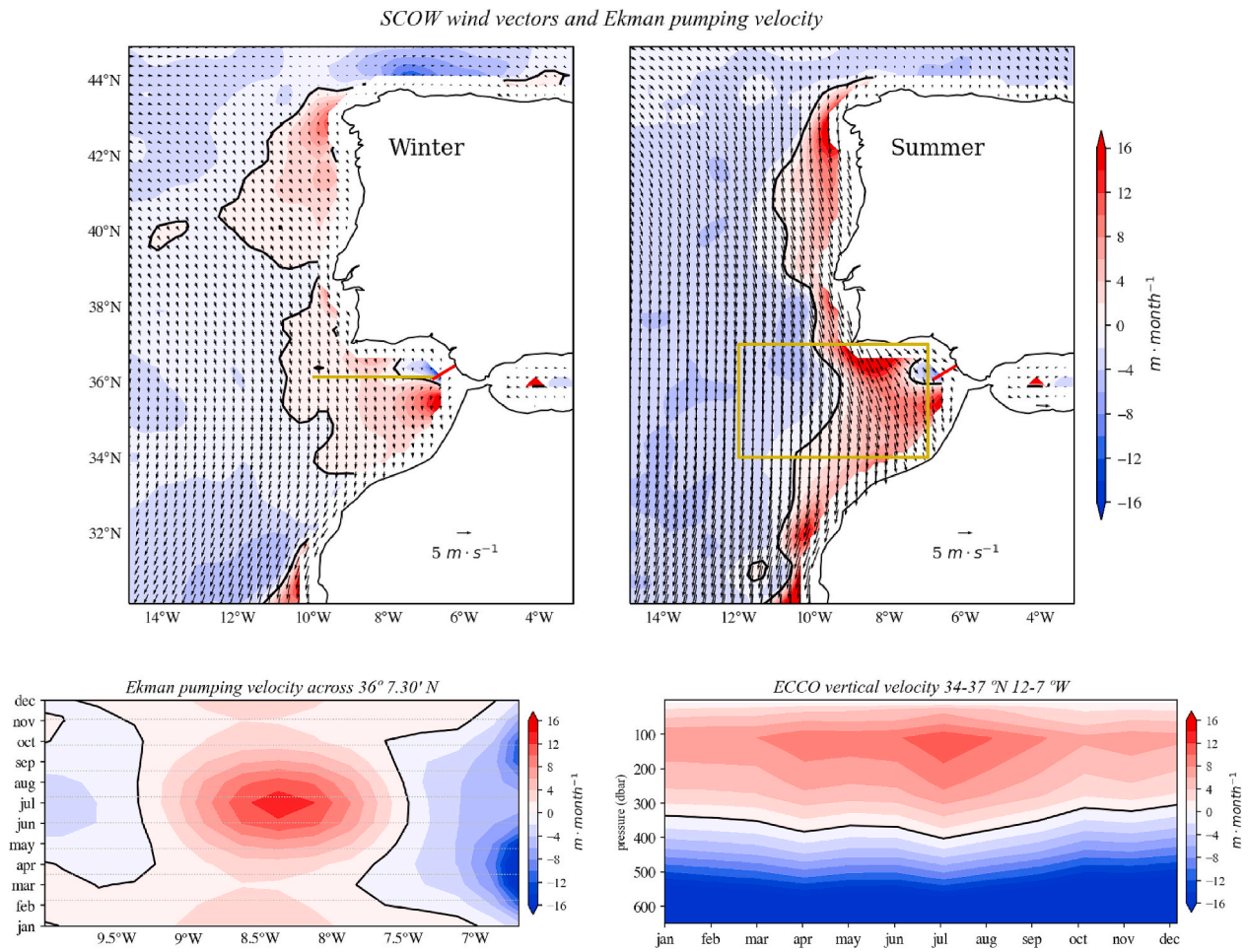

Fig. 11.(Top) Ocean wind vectors (m skg m^{-3}-1) over Ekman pumping velocity (m month^{-1}) from the SCOW climatology (Risien and Chelton, 2008). The top-left panel illustrates the winter (DFM) average. The top-right panel shows the summer (JJA) average. A red line indicates the location of SP line. (Bottom-left) Climatology of the Ekman pumping velocity along 36° 07′N (yellow line in the top-left panel). (Bottom-right) Seasonal variations of the vertical velocity from ECCO, spatially averaged over the yellow box indicated in the top-right panel. (For interpretation of the references to color in this figure legend, the reader is referred to the Web version of this article.)Fig

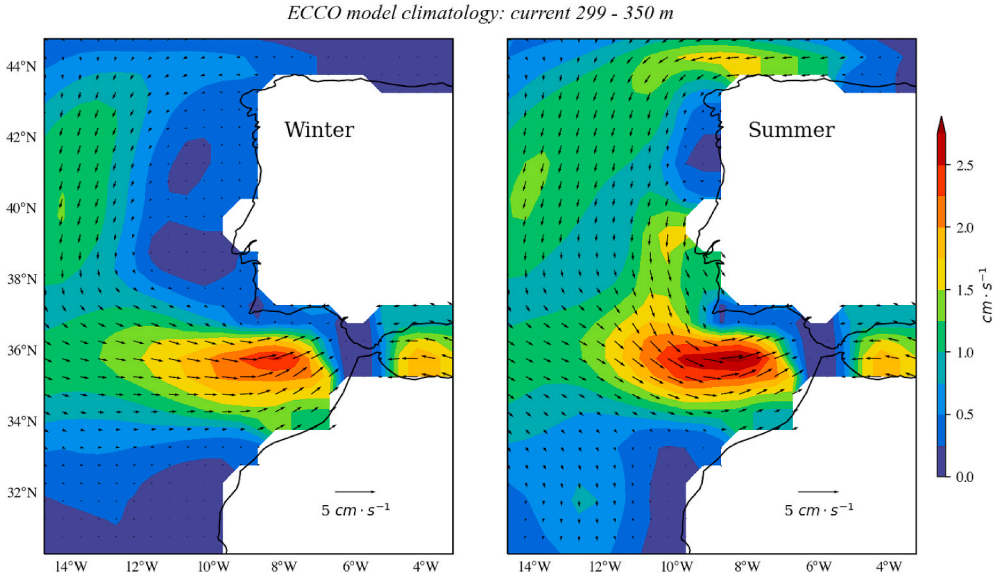

Fig. 12. ECCO current velocity vectors averaged over 299–350 m (l-ENACW layer) in winter (DFM; left panel) and summer (JJA; right panel). Color shades depict the current velocity. (For interpretation of the references to color in this figure legend, the reader is referred to the Web version of this article.)

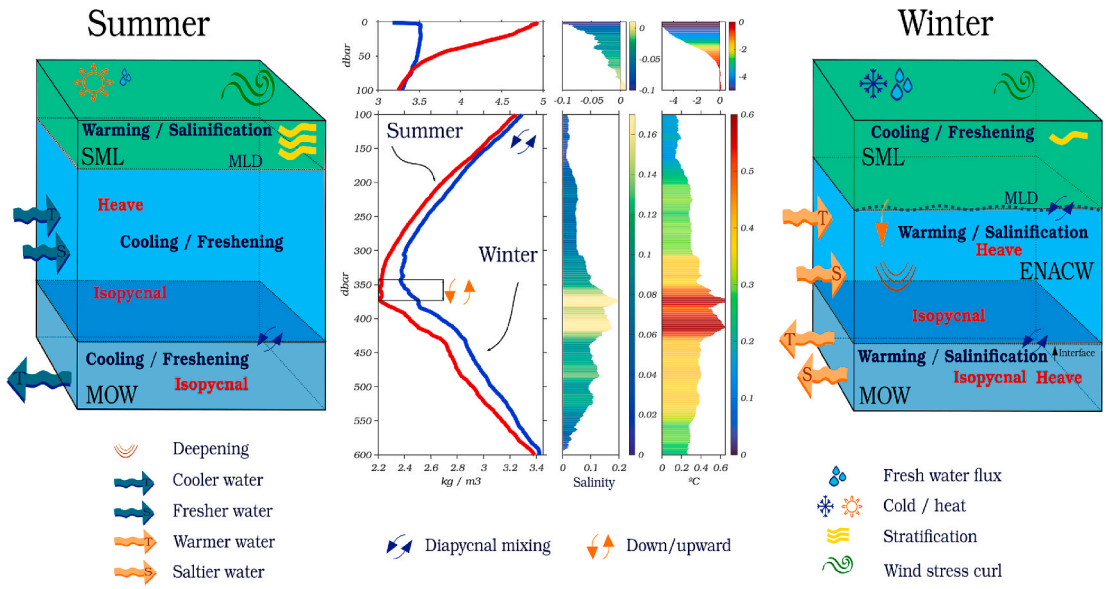

Fig. 13. Sketch illustrating the seasonality of thermohaline changes across the water column in the northern GoC. Bold types (in black) indicate the sign and source of the change in a particular depth interval. The direction of horizontal and vertical advection of heat and freshwater, as well as the driving mechanism deduced from this study and the literature review, were outlined as colored arrows, as indicated in the legend below. The central panel presents the mean winter and summer spiciness vertical profiles, as well as winter-summer salinity (central) and temperature (right) differences (colorbars represent the magnitude). The water column below 100 m is spicier in winter. Maximum differences occur below 300 m, specially across the deeper part of the l-ENACW core, which is > 0.6 ˚C warmer, > 0.15 more saline and about 25 m shallower in winter.

4.2. MOW

Thermohaline changes across the upper MOW occur approximately in phase with those in the overlying l-ENACW. Temperature is primarily controlled by the isopycnal term, but heave is equally important for salinity. The possible causes of these seasonal differences should respond to variations of: i) the volume and strength of the overflow (these would emerge as vertical displacements of isopycnals); and/or ii) the water masses involved in the MOW production (isopycnal changes).

Topographic control (Liang et al., 2017) and entrainment García--Lafuente et al. (2015) are relevant to control vertical velocities near the bottom. Entrainment steer year-round downward heaving within the MOW (Fig. 11, bottom-right panel). Decomposition of salinities at SP6 suggest downward heaving below 550 m (below 500 m in autumn; Fig. 9), although except for autumn, this downward heaving has little effect on the isobaric change, probably because of the topographic control of the Mediterranean undercurrent across SP.

The thickness of the ENACW layer in the GoC undergoes seasonal changes (Bormans et al., 1986). Maximum elevation of the l-ENACW/-MOW interface at ES occurs between April/June (192 m) and minimum (200 m) between September/November, including a 10% percent change of the MOW volume transport (Sammartino et al., 2015). That is equivalent to the periodic alteration of the rate of water mass renewal in subduction areas, which may emerge as heave changes (*e.g.,* Desbruyères et al., 2014). The similarity with the seasonal cycle of heave for MOW salinity (Fig. 10) suggests a common driving mechanism. However, the absence of a clear heave cycle for temperature suggests the stronger importance of isopycnal changes.

Mediterranean waters in the eastern SoG exhibit the remote response to seasonal formation of Winter Mediterranean Deep Water (WMDW) in the Gulf of Lion (García-Lafuente et al., 2007). The mechanism is related with the uplift of cooler waters in Alborán by newer WDMW vintages and posterior suction towards the SoG (García-Lafuente et al., 2009; Naranjo et al., 2012, 2017). The consequence is that waters flowing out of the Mediterranean sea exhibit a temperature drop of about 0.04 ˚C between March–May, which is marginally detected in ES_{moor} data (Naranjo et al., 2017). Rather, a seasonal cycle similar to that of Atlantic waters prevails (winter-summer differences of about 0.08 ˚C; Naranjo et al., 2017, their Fig. 3). Entrainment of 0.03 Sv Atlantic waters in the Tangier basin (TB) induces changes to the properties of the outflow between ES and CS (García-Lafuente et al., 2011) that likely erode any seasonal signature of pure MedW. In fact, assuming full mix during entrainment, seasonal differences of 1 ˚C in Atlantic waters suffice to override the seasonal temperature changes of pure MedW.

MedW types at ES distribute along the side of the triangle joining u- ENACW and MedW (Fig. 3). This indicates that u-ENACW is the primary source of water entrained by the outflow throughout TB. West of Spartel, MOW types are rather sorted on the line bisecting the mixing triangle, suggesting an increasing proportion of l-ENACW. Sánchez-Leal et al. (2017) estimated that 70% of the MOW volume transport across SP correspond to ENACW entrained by the overflow. Assuming full mix between MOW and Atlantic waters, l-ENACW summer-winter differ-ences of 0.5 ˚C would result in MOW temperature changes of approxi-mately 0.3 ˚C, which is what we observe at SP6 (Fig. 10 and Table 1). These changes exceed by one order of magnitude the seasonal cycle of the purest MedW at ES.

MOW temperature variations at SP6 are accompanied by coeval winter-summer salinity differences (0.1; Fig. 10 and Table 1). These cannot be attributable to changes at ES (Naranjo et al., 2017). Rather, the source of variations at SP6 stands in the variability of l-ENACW in the GoC. In fact, l-ENACW salinity differences of 0.14 (Fig. 10 and Table 1) would result in a total change of about 0.1 at SP6, which is in agreement with our observations. Summer increment of l-ENACW on the upper slope (Fig. 8) and subsequent transport towards the eastern GoC by the GCC (Peliz et al., 2009) accounts for the variability of waters entrained by the outflow, which must be held responsible for seasonal variability of the MOW west of the SoG.

5. Summary and conclusions

This work describes the seasonal thermohaline variability in the northeastern Gulf of Cádiz based on the analysis of more than ten years of repeated hydrographic observations. We discussed the physical processes steering the seasonal cycle of Eastern North Atlantic Central

(ENACW) and Mediterranean Overflow Waters (MOW). Results are summarized in Fig. 13.

The most outstanding finding is the presence of a strong seasonal signal emanating from the l-ENACW core that is mirrored by the underlying MOW layer. The discussed mechanisms are the horizontal and vertical advection related to the seasonal cycle of the wind stress and its curl west of the Iberian Peninsula. The former steers the seesaw between poleward-equatorward transports and explains the alternating sign of the isopycnal change at the l-ENACW core. The latter is responsible for heave-steered changes above.

Ekman pumping is positive throughout the year but intensifies in spring-summer, in parallel with the onset of the upwelling-favorable season. It steers positive vertical velocities at the base of the seasonal thermocline and contributes to the elevation of isopycnals above 350 m. It results in summer cooling and freshening at the u-ENACW level. Upwelling-favorable winds also stimulate the penetration of equatorward flows from the coastal branch of the Portugal Current System. This also occurs in spring-summer, coeval with the seasonal extension of the North Atlantic Subtropical Gyre that permits the entrance of relatively cool, low salinity waters into the GoC. Warming and salinification in autumn is explained by the relaxation of upwelling-favorable winds. The shift of the current system facilitates deeper infiltration of the Azores Current bringing warmer, more saline subtropical waters at intermediate levels.

Thermohaline changes in the MOW layer occur in phase and sign with those across the l-ENACW. The MOW is a mixing product of about 40% MedW and 60% Atlantic waters (about 30% l-ENACW and 30% u-ENACW). Results suggest that during the early transformation stages the MOW current primarily entrains u-ENACW (and waters from the surface mixed layer in severe winters). Past Espartel sill, l-ENACW is actively incorporated by the overflow current. Due to efficient mixing and given the larger ranges of seasonal variability of Atlantic waters, the latter is more influential on the composition of the upper MOW than the variability of MedW leaving the Mediterranean Sea. This mechanism of seasonal modulation of MOW properties may be relevant in a warming climate scenario. The continuity of the observational effort such as the one presented here, is of particular importance to consolidate and improve our understanding of the long-term variability of such a relevant water mass at the site of production.

Declaration of competing interest

The authors declare that they have no known competing financial interests or personal relationships that could have appeared to influence the work reported in this paper.

Acknowledgments

Data presented here were acquired during dedicated STOCA cruises as well as during cruises of opportunity. We thank Fernando Ramos (Chief Scientist) for his unwavering support during ECOCADIZ and ECOCADIZ-RECLUTAS surveys. We are indebted to IEO, GOFIMA (Physical Oceanography Group of the University of Malaga) and ICMAN-CSIC technicians that took part in the data acquisition. We are indebted to the crews of the R/V's Cornide de Saavedra, Ángeles Alvariño, Ramón Margalef and Miguel Oliver. We thank E. Prieto, V. Benítez-Barrios and two anonymous reviewers for their valuable comments, which greatly improved an earlier version of the manuscript. M.J.B. thanks the financial support from the Spanish Institute of Oceanography (IEO) PhD grant IEO-FPI 2011/10. C.N. acknowledges the postdoctoral fellowship from the University of Malaga. This is a contribution to STOCA (IEO2009), PESCADIZ (IEO2008), PELCOSAT-3 (IEO2012), INGRES3 (CTM2010-21229), DILEMA (CTM2014-59244-C3-2-R), INPULSE (CTM2016-75129-C3-1-R) and OCASO (INTERREG-POPTEC 0223_OCASO_5_E) projects. This manuscript was finished thanks to teleworking during COVID-19 lockdown. STOCA/GoCaTS metadata can be accessed through the SeaDataNet portal https://cdi.seadatanet.org/search. Data are available from the corresponding author on reasonable request.

Appendix A. Supplementary data

Supplementary data to this article can be found online at https://doi.org/10.1016/j.csr.2020.104190.

References

Arbic, B.K., Owens, W., 2001. Climatic warming of atlantic intermediate waters. J. Clim. Am. Meteorol. Soc. 14.

Baringer, M.O., Price, J.F., 1997. Mixing and spreading of the mediterranean outflow. J. Phys. Oceanogr. 27 (8), 1654–1677.

Bellanco, M., Sánchez-Leal, R., 2016. Spatial distribution and intra-annual variability of water masses on the Eastern Gulf of Cádiz seabed. Continent. Shelf Res. 128, 26–35.

Bindoff, N.L., McDougall, T.J., 1994. Diagnosing climate change and ocean ventilation using hydrographic datas. J. Clim. Am. Meteorol. Soc. 24.

Bormans, M., Garrett, C., Thompson, K., 1986. Seasonal variability of the surface inflow through the Strait of Gibraltar. Oceanol. Acta 9 (4), 403–414.

Bozec, A., Lozier, M.S., Chassignet, E.P., Halliwell, G.R., 2011. On the variability of the mediterranean outflow water in the north atlantic from 1948 to 2006. J. Geophys. Res.: Oceans 116 (C9).

Carracedo, L., Gilcoto, M., Mercier, H., Pérez, F., 2014. Seasonal dynamics in the Azores–Gibraltar strait region: a climatologically-based study. Prog. Oceanogr. 122, 116–130, 0.

Carracedo, L.I., Pardo, P.C., Flecha, S., Pérez, F.F., 2016. On the mediterranean water composition. J. Phys. Oceanogr. 46 (4), 1339–1358.

Carton, X., Daniault, N., Alves, J., Cherubin, L., Ambar, I., 2010. Meddy dynamics and interaction with neighboring eddies southwest of Portugal: observations and modeling. J. Geophys. Res.: Oceans 115 (C6).

Chen, G., Wang, X., 2016. Vertical structure of upper-ocean seasonality: annual and semiannual cycles with oceanographic implications. J. Clim. 29 (1), 37–59.

Desbruyères, D.G., McDonagh, E.L., King, B.A., Garry, F.K., Blaker, A.T., Moat, B.I., Mercier, H., 2014. Full-depth temperature trends in the northeastern atlantic through the early 21st century. Geophys. Res. Lett. 41 (22), 7971–7979.

Flament, P., 2002. A state variable for characterizing water masses and their diffusive stability: spiciness. Prog. Oceanogr. 54 (1–4), 493–501.

Forget, G., Campin, J.-M., Heimbach, P., Hill, C.N., Ponte, R.M., Wunsch, C., 2015. Ecco version 4: an integrated framework for non-linear inverse modeling and global ocean state estimation. Geosci. Model Dev. (GMD) 8 (10), 3071–3104.

García-Lafuente, J., Sánchez-Román, A., Naranjo, C., Sánchez-Garrido, J.C., 2011. The very first transformation of the mediterranean outflow in the strait of Gibraltar. J. Geophys. Res.: Oceans 116 (C7).

García-Lafuente, J., Delgado, J., Sánchez Román, A., Soto, J., Carracedo, L., Díaz del Río, G., 2009. Interannual variability of the Mediterranean outflow observed in Espartel sill, western Strait of Gibraltar. J. Geophys. Res.: Oceans 114 (C10), c10018 n/a–n/a.

García-Lafuente, J., Naranjo, C., Sammartino, S., Sánchez-Garrido, J.C., Delgado, J., 2017. The mediterranean outflow in the strait of Gibraltar and its connection with upstream conditions in the alborán sea. Ocean Sci. 13 (2), 195–207.

García-Lafuente, J., Naranjo, C., Sánchez-Leal, R., Sammartino, S., Bellanco, M.J., Sánchez-Garrido, J.C., Soto-Navarro, J., 2015. On the origin of the seasonal and interannual T–S variability of the inflow through the Strait of Gibraltar. Deep Sea Res. Pap. I 101, 38–53.

García-Lafuente, J., Sánchez Román, A., Díaz del Río, G., Sannino, G., Sánchez Garrido, J.C., 2007. Recent observations of seasonal variability of the Mediterranean outflow in the Strait of Gibraltar. J. Geophys. Res.: Oceans 112 (C10), n/a–n/a.

González-Pola, C., Fratantoni, P., Larsen, K.M.H., Holliday, N.P., Dye, S., Mork, K.A., Beszczynska-Möller, A., Valdimarsson, H., Trofimov, A., Parner, H., Klein, H., Cisewski, B., Fontán, A., Lyons, K., Kolodziejczyk, N., Graña, R., Linders, J., Wodzinowski, T., Goszczko, I., Cusack, C., 2019. The ices working group on oceanic hydrography: a bridge from in-situ sampling to the remote autonomous observation era. Front. Mar. Sci. 6, 103.

Hernández-Molina, F.J., Stow, D.A.V., Alvarez-Zarikian, C.A., Acton, G., Bahr, A., Balestra, B., Ducassou, E., Flood, R., Flores, J.-A., Furota, S., Grunert, P., Hodell, D., Jimenez-Espejo, F., Kim, J.K., Krissek, L., Kuroda, J., Li, B., Llave, E., Lofi, J., Lourens, L., Miller, M., Nanayama, F., Nishida, N., Richter, C., Roque, C., Pereira, H., Sanchez Goñi, M.F., Sierro, F.J., Singh, A.D., Sloss, C., Takashimizu, Y., Tzanova, A., Voelker, A., Williams, T., Xuan, C., 2014. Onset of mediterranean outflow into the north atlantic. Science 344 (6189), 1244–1250.

Iorga, M.C., Lozier, M.S., 1999. Signatures of the mediterranean outflow from a north atlantic climatology: 1. salinity and density fields. J. Geophys. Res.: Oceans 104 (C11), 25985–26009.

Leadbetter, S.J., Williams, R.G., McDonagh, E.L., King, B.A., 2007. A twenty year reversal in water mass trends in the subtropical north atlantic. Geophys. Res. Lett. 34 (12).

Liang, X., Spall, M., Wunsch, C., 2017. Global ocean vertical velocity from a dynamically consistent ocean state estimate. J. Geophys. Res.: Oceans 122 (10), 8208–8224.

Louarn, E., Morin, P., 2011. Antarctic intermediate water influence on mediterranean sea water outflow. Deep Sea Res. Oceanogr. Res. Pap. 58 (9), 932–942.

Machín, F., Pelegrí, J., Marrero-Díaz, A., Laiz, I., Ratsimandresy, A., 2006. Near-surface circulation in the southern gulf of cádiz. Deep Sea Res. Part II Top. Stud. Oceanogr. 53 (11–13), 1161–1181.

Mamayev, O.I., 1, 1975. Temperature-Salinity Analysis of World Ocean Waters, first ed., 11 of 10. Elsevier Scientific Publishing.

Mason, E., Colas, F., Molemaker, J., Shchepetkin, A.F., Troupin, C., McWilliams, J.C., Sangrà, P., 2011. Seasonal variability of the Canary Current: a numerical study. J. Geophys. Res.: Oceans 116 (C6), c06001 n/a–n/a.

Mauritzen, C., Morel, Y., Paillet, J., 2001. On the influence of mediterranean water on the central waters of the north Atlantic ocean. Deep Sea Res. Oceanogr. Res. Pap. 48 (2), 347–381.

McDougall, T.J., Krzysik, O.A., 2015. Spiciness. J. Mar. Res. 73 (5).

McTaggart, K., Johnson, G., Delahoyde, M., Swift, J., 2010. Notes on ctc/o2 data acquisition and processing using sea-bird hardware and software (as available). In: Hood, E., Sabine, C., Sloyan, B. (Eds.), The GO-SHIP Repeat Hydrography Manual: A Collection of Expert Reports and Guidelines. Version 1. IOCCP Report Number 14, ICPO Publication Series. Number 134, p. 10, an optional note.

Millot, C., 2007. Interannual salinification of the Mediterranean inflow. Geophys. Res. Lett. 34 (21), l21609 n/a–n/a.

Naranjo, C., García-Lafuente, J., Garrido, J.C.S., Román, A.S., Cabello, J.D., 2012. The western alboran gyre helps ventilate the western mediterranean deep water through Gibraltar. Deep Sea Res. Oceanogr. Res. Pap. 63, 157–163, 0.

Naranjo, C., García-Lafuente, J., Sammartino, S., Sánchez-Garrido, J.C., Sánchez-Leal, R., Bellanco, M., 2017. Recent changes (2004–2016) of temperature and salinity in the Mediterranean outflow. Geophys. Res. Lett. 44 (11), 5665–5672, 2017GL072615.

Naranjo, C., Sammartino, S., García-Lafuente, J., Bellanco, M.J., Taupier-Letage, I., 2015. Mediterranean waters along and across the Strait of Gibraltar, characterization and zonal modification. Deep Sea Res. Oceanogr. Res. Pap. 105, 41–52.

Peliz, A., Boutov, D., Teles-Machado, A., 2013. The alboran sea mesoscale in a long term high resolution simulation: statistical analysis. Ocean Model. 72, 32–52.

Peliz, A., Dubert, J., Marchesiello, P., Teles-Machado, A., 2007. Surface circulation in the Gulf of Cadiz: model and mean flow structure. J. Geophys. Res.: Oceans 112 (C11).

Peliz, A., Marchesiello, P., Santos, A.M.P., Dubert, J., Teles-Machado, A., Marta-Almeida, M., Le Cann, B., 2009. Surface circulation in the gulf of cadiz: 2. Inflow-outflow coupling and the gulf of cadiz slope current. J. Geophys. Res.: Oceans 114 (C3).

Potter, R.A., Lozier, M.S., 2004. On the warming and salinification of the Mediterranean outflow waters in the North Atlantic. Geophys. Res. Lett. 31 (1).

Prieto, E., González-Pola, C., Lavín, A., Sánchez, R.F., Ruiz-Villarreal, M., 2013. Seasonality of intermediate waters hydrography west of the Iberian Peninsula from an 8 yr semiannual time series of an oceanographic section. Ocean Sci. 9 (2), 411–429.

Relvas, P., Barton, E.D., 2002. Mesoscale patterns in the cape são vicente (iberian Peninsula) upwelling region. J. Geophys. Res.: Oceans 107 (C10), 28–1–28–23.

Risien, C.M., Chelton, D.B., 2008. A global climatology of surface wind and wind stress fields from eight years of QuikSCAT scatterometer data. J. Phys. Oceanogr. 38 (11), 2379–2413.

Roque, D., Parras-Berrocal, I., Bruno, M., Sánchez-Leal, R., Hernández-Molina, F.J., 2019. Seasonal variability of intermediate water masses in the gulf of cádiz: implications of the antarctic and subarctic seesaw. Ocean Sci. 15 (5), 1381–1397.

Sammartino, S., García Lafuente, J., Naranjo, C., Sánchez Garrido, J.C., Sánchez Leal, R., Sánchez Román, A., 2015. Ten years of marine current measurements in Espartel Sill, Strait of Gibraltar. J. Geophys. Res.: Oceans 120, 6309–6328 n/a–n/a.

Sánchez, R.F., Relvas, P., 2003. Spring–summer climatological circulation in the upper layer in the region of Cape St. Vincent, Southwest Portugal. ICES (Int. Counc. Explor. Sea) J. Mar. Sci.: J. Conseil. 60 (6), 1232–1250.

Sánchez-Leal, R.F., Bellanco, M.J., Fernández-Salas, L.M., García-Lafuente, J., Gasser-Rubinat, M., González-Pola, C., Hernández-Molina, F.J., Pelegrí, J.L., Peliz, A., Relvas, P., Roque, D., Ruiz-Villarreal, M., Sammartino, S., Sánchez-Garrido, J.C., 2017. The mediterranean overflow in the gulf of cadiz: a rugged journey. Sci. Adv. 3 (11).

Schmitt, R.W., 1999. Spice and the demon. Science 283 (5401), 498–499.

Stramma, L., Siedler, G., 1988. Seasonal changes in the North Atlantic subtropical gyre. J. Geophys. Res.: Oceans 93 (C7), 8111–8118.

Swingedouw, D., Colin, C., Eynaud, F., Ayache, M., Zaragosi, S., 2019. Impact of freshwater release in the Mediterranean sea on the north atlantic climate. Clim. Dynam. 53 (7), 3893–3915.

Tel, E., Balbín, R., Cabanas, J.-M., García, M.-J., García-Martínez, M.C., González-Pola, C., Lavín, A., Lopez-Jurado, J.-L., Rodríguez, C., Ruiz-Villarreal, M., Sánchez-Leal, R.F., Vargas-Yáñez, M., Vélez-Belchí, P., 2016. IEOOS: the Spanish Institute of Oceanography observing system. Ocean Sci. 12 (2), 345–353.

Teles-Machado, A., Peliz, A., McWilliams, J.C., Cardoso, R.M., Soares, P.M.M., Miranda, P.M.A., 2015. On the year-to-year changes of the iberian poleward current. J. Geophys. Res.: Oceans 120 (7), 4980–4999.

van Dijk, J., Ziegler, M., de Nooijer, L.J., Reichart, G.J., Xuan, C., Ducassou, E., Bernasconi, S.M., Lourens, L.J., 2018. A saltier glacial mediterranean outflow. Paleoceanogr. Paleoclimatol. 33 (2), 179–197.